

Available online at www.sciencedirect.com**ScienceDirect**journal homepage: www.elsevier.com/locate/he**ELSEVIER**

A comprehensive 3-D modeling of a single planar solid oxide fuel cell

**Marko Nerat^{*}, Đani Jurčić**

Jožef Stefan Institute (JSI), Jamova 39, SI-1000 Ljubljana, Slovenia

ARTICLE INFO**Article history:**

Received 30 July 2015

Received in revised form

20 November 2015

Accepted 23 November 2015

Available online 8 January 2016

Keywords:

Conversion efficiency

Fuel utilization

Internal methane steam reforming

Solid oxide fuel cell (SOFC)

Temperature gradients

Three-dimensional (3-D) modeling

ABSTRACT

The main motivation of the presented paper is to study the amplitude and location of the maximum temperature (T_{\max}) and maximum temperature gradient ($\Delta T/\Delta x_{\max}$), respectively, as well as the performance parameters of the modeled, single, planar, anode-supported, solid oxide fuel cell (SOFC) with internal methane steam reforming at different operating conditions (i.e. current density and inlet velocity of fuel gas). The reforming reaction and locally increased current density lead to inhomogeneous heat generation within the SOFC that results in inhomogeneous distribution of temperature. Due to the latter, a comprehensive, three-dimensional, thermo-fluid model of the SOFC has been developed and implemented in software package COMSOL Multiphysics® 4.3. The simulation results show that the amplitude and location of the T_{\max} and $\Delta T/\Delta x_{\max}$ within the modeled SOFC depend on operating conditions. The data about their values can be efficiently used instead of temperature measurements with expensive embedded thermocouples when a realistic, operating SOFC is controlled. The results also show that the current density and the inlet velocity of fuel gas are the key parameters to improve the fuel utilization and the total conversion efficiency.

Copyright © 2015, Hydrogen Energy Publications, LLC. Published by Elsevier Ltd. All rights reserved.

Introduction

Fuel cells (FCs) have become attractive as alternative power sources during the last decades since they convert chemical energy of the fuel directly into electrical energy with high conversion efficiency [1]. Some FCs must be supplied with pure hydrogen as a fuel, e.g. proton exchange membrane (PEM) FCs, which operate at low temperatures ($T < 100^{\circ}\text{C}$), whereas the others can be supplied with different mixtures of fuels, with e.g. hydrogen, methane, natural gas, and carbon monoxide [2]. One of practically interesting FCs, which can be supplied with hydro-carbon fuels, are solid oxide fuel cells (SOFCs), which

operate at high temperatures ($T = 650\text{--}1000^{\circ}\text{C}$) [3]. The SOFC consists of a positive electrode (cathode), solid oxide (electrolyte) and negative electrode (anode) sandwiched between the metal contacts, as can be seen in Fig. 1a. The contacts are commonly made of ferritic (Fe) alloys with chrome (Cr) or nickel (Ni). They serve to conduct electric current from the cathode to the external load and from the load back to the anode, or to interconnect many cells in parallel or/and in series into the stack. Besides this, the contacts form the fuel- and air-flow channel adjacent to the anode and cathode side of the SOFC, respectively. The anode is usually porous nickel/yttria-stabilized zirconia (Ni/YSZ) material, the electrolyte is dense YSZ and the cathode is porous lanthanum manganite (LaMnO_3)

* Corresponding author. Tel.: +386 14773240; fax: +386 14773994.

E-mail address: marko.nerat@ijs.si (M. Nerat).

<http://dx.doi.org/10.1016/j.ijhydene.2015.11.136>

0360-3199/Copyright © 2015, Hydrogen Energy Publications, LLC. Published by Elsevier Ltd. All rights reserved.

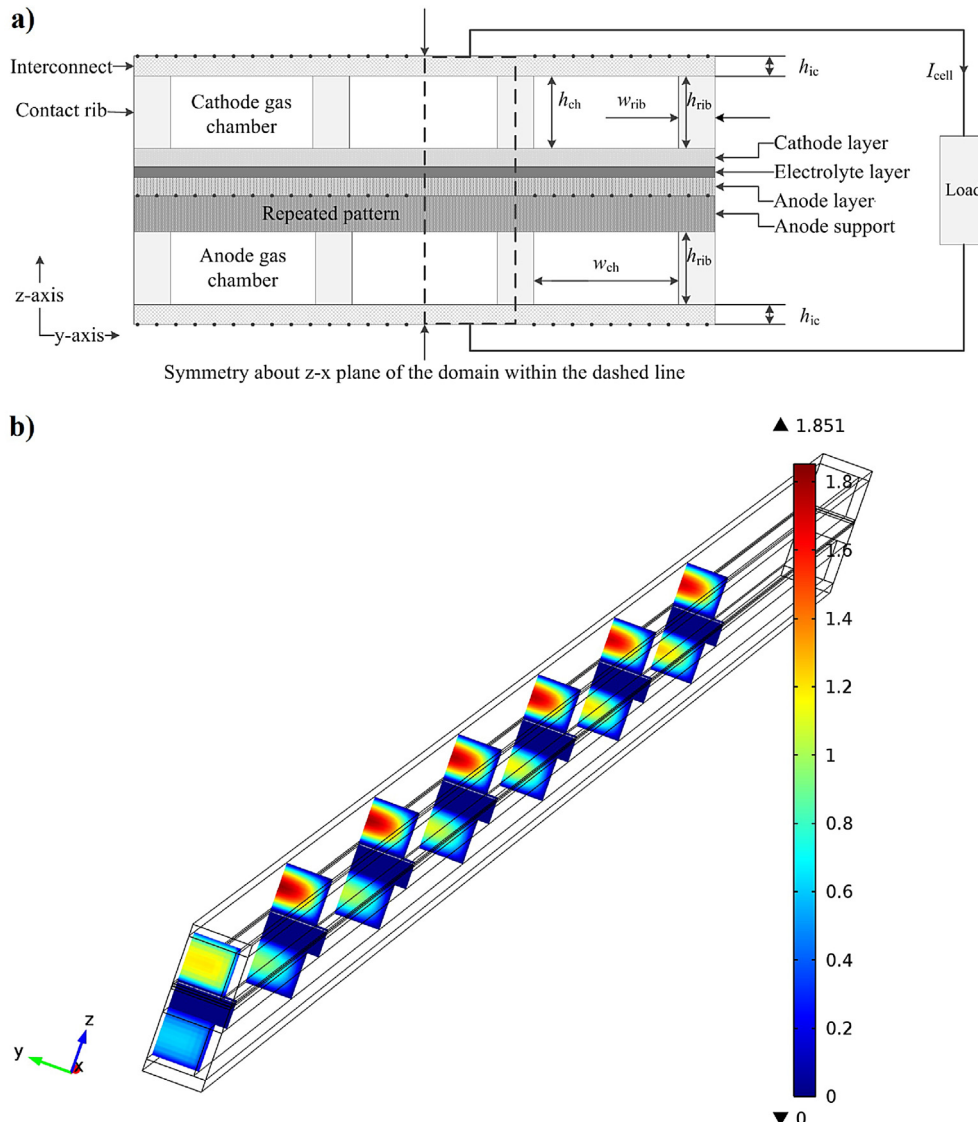


Fig. 1 – a) Cross-section profile of the modeled solid oxide fuel cell (SOFC) with external load, **b)** Velocity field (in m s^{-1}) of gas species in the modeled SOFC structure.

doped with strontium (LSM) [4]. Under the operation of SOFC (i.e. the FC is supplied with inflow of air and fuel), the following electrochemical reactions occur within triple phase boundaries (TPBs are thin boundaries between the electrode and electrolyte micrograins surrounded with gaseous phases that fill the pores) at the interfaces between the electrolyte and cathode (1 – reduction), and electrolyte and anode (2, 3 – oxidation) catalyst layer:



The oxygen is thus adsorbed within the TPBs at the interface between the electrolyte and porous cathode and the oxygen ions are transferred through the dense electrolyte to the

interface between the electrolyte and porous anode, where the oxidation of hydrogen/carbon monoxide occurs within the TPBs. The flow of oxygen ions through the electrolyte represents electric current density that is in the opposite direction since the ions are negatively charged. The flow of electrons is terminated through the load, which is connected to the contacts, and it represents the output current density of the SOFC. The electrons exit the anode side and enter the cathode side of the SOFC through the contacts and load. The output current density is thus directed from cathode to anode side through the electric load since electrons are negatively charged. The physical background behind the operation of a SOFC is far more complex as explained before and cannot be described in all details at this point.

In this paper, the study is based on physical model that consist of coupled partial differential equations when spatial variations of dependent variables are considered. The models are conditioned by the purpose of application. Many different

studies employing modeling have been conducted recently and have focused on various geometries [1] and operating conditions [5] of anode-supported cells [6–8] with internal [6,7] or external [8] reforming of methane. The reforming of methane is endothermic reaction that consumes the heat and possibly leads to locally lowered temperature within the porous anode layer [6]. The results show high temperature gradients along the fuel- and/or airflow channels when the reforming occurs. However, the models in Refs. [6,7] are simplified to one- or two-dimensional variation of temperature rather than representing complete three-dimensional variation. The three-dimensional diffusion of gases through the porous electrodes is also neglected. The model of SOFC with internal reforming, which is presented in Ref. [9], is complex, since it includes charge, species, mass, momentum and energy conservation equations in three dimensions.

However, the modeled steam reforming reaction is simplified since it considers only the methane's partial pressure. There are many other models that can be found in the literature, but they are limited to a specific structure [10], or are too complex to be implemented on device level since the electrochemistry [11] and transport [11,12] phenomena are modeled on microscale level.

The purpose of this work is to build an advanced, steady state, three-dimensional (3-D) model of a single, planar, anode-supported SOFC with internal reforming. In this study, the model of steam reforming considers forward and backward reactions, which are dependent on partial pressures of methane, water vapor, hydrogen and carbon monoxide. Furthermore, the heat transfer model includes thermal radiation through the SOFC's surface since it is assumed that a single cell operates within the sealed chamber and the radiative heat transfer is important. The resistance of the contacts with interconnects is also included in this model. Besides this, two modeling approaches, with and without thermal radiation through the SOFC's surface, are presented and discussed in terms of the simulation results accuracy.

The main goal of this study is to obtain valuable data about the amplitude and location of the maximum temperature (T_{\max}) and maximum temperature gradients ($\Delta T/\Delta x_{\max}$) within the modeled SOFC. The data is important when the control of a realistic SOFC is performed since the number of expensive embedded thermocouples for local temperature measurements can be considerably reduced or even zero. Moreover, the amplitude and location of the T_{\max} (and $\Delta T/\Delta x_{\max}$) within a realistic SOFC depend on operating conditions. Consequently, the measurements of local temperature might not reproduce the exact T_{\max} ($\Delta T/\Delta x_{\max}$) due to a fixed spatial position of embedded thermocouples. The main novelty, or the main contribution, of this paper is thus using the 3-D model of SOFC to study temperature profiles and gradients within the SOFC to obtain data about T_{\max} and $\Delta T/\Delta x_{\max}$ instead of using simplified 1-D (2-D) models or linear interpolation.

Modeling

A three-dimensional (3-D) model of a single, planar, anode-supported SOFC is developed and implemented in software

package COMSOL Multiphysics® 4.3. The model includes charge, species, mass, momentum and energy transport conservation equations that can be found in literature [10]. However, some differences exist in the presented model and these are outlined.

Geometry and meshing

The modeled SOFC structure consist of porous electrodes and solid oxide (thin electrolyte layer sandwiched in between thin active cathode and anode layer, supported with thicker porous anode layer), connected to external electric load through the contacts, as schematically shown in cross-section profile in Fig. 1a. The dimensions of the modeled SOFC including its layers are listed in Table 1 and are similar to those found in the literature [10,13].

It should be pointed out that computational domain, indicated with dashed line in Fig. 1a, includes only a periodic part of the modeled structure and the symmetry about the z-x plane is considered to reduce memory usage and computational time during the simulations. Obviously, appropriate boundary conditions for symmetry have to be considered at the left and right surface (in parallel to the z-x plane) of the computational domain.

The computational domain is meshed with 31000 ($l \times w \times h = 50 \times 10 \times 62$) finite volume elements, as can be seen in Table 2. Please note that computational domain consists of two contact ribs (2×10 elements) and two interconnects (2×5 elements). Increasing or decreasing the number of elements by a factor of two in arbitrary direction (along the x-, y- or z-axis) influences the solution accuracy by a few percent only, so the meshing from Table 2 is adopted.

Model description

A three-dimensional (3-D), steady state, thermo-fluid model coupled with electrochemical and reforming reactions for a single, planar, anode-supported, SOFC has been developed to study current densities, electrostatic field, transport of gases, temperature distributions and reaction rates within the computational domain. The model is composed of eight sub-domains, namely two gas chambers, two porous electrodes, two porous catalyst layers (anode and cathode, respectively), the electrolyte and contacts with interconnects, that are

Table 1 – Dimensions of the modeled SOFC.

Dimensions	Values (m)
Cell length (x-axis), l	1.0×10^{-1}
Cell width (y-axis), w	1.0×10^{-1}
Cathode/anode gas chamber width (y-axis), w_{ch}	2.0×10^{-3}
Cathode/anode gas chamber height (z-axis), h_{ch}	1.0×10^{-3}
Contact rib width (y-axis), w_{rib}	5.0×10^{-4}
Contact rib height (z-axis), h_{rib}	1.0×10^{-3}
Interconnect height (z-axis), h_{ic}	2.5×10^{-4}
Cathode active layer thickness (z-axis), d_c	5.0×10^{-5}
Electrolyte layer thickness (z-axis), d_e	1.0×10^{-5}
Anode active layer thickness (z-axis), d_a	5.0×10^{-5}
Anode support layer thickness (z-axis), d_s	5.0×10^{-4}

Table 2 – Meshing of the structure.

Dimensions	Number of elements
Cell length (x-axis), l	50
Cathode/anode gas chamber width (y-axis), w_{ch}	8
Cathode/anode gas chamber height (z-axis), h_{ch}	10
Contact rib width (y-axis), w_{rib}	2
Contact rib height (z-axis), h_{rib}	10
Interconnect height (z-axis), h_{ic}	5
Cathode active layer thickness (z-axis), d_c	5
Electrolyte layer thickness (z-axis), d_e	2
Anode active layer thickness (z-axis), d_a	5
Anode support layer thickness (z-axis), d_s	20

governed by appropriate equations and boundary conditions. The equations and boundary conditions have to be parameterized with corresponding parameters used in the model.

Gas chambers

The gas chamber is patterned with contact ribs and interconnects that form a rectangular duct together with porous anode support layer or porous cathode layer, as can be seen in Fig. 1a. The flow of gases is assumed steady and is modeled according to Equations (3)–(12) in Ref. [10]. The important issues when modeling the fluxes and heat exchange are physical properties of gas species that are involved at these processes. Thus, the following viscosities, thermal conductivities and specific heats at constant pressure are adopted from literature [14–17] and are shown in Table 3. As can be seen, all these quantities are linearized functions of temperature T , that approximate measured values in the range from 800 °C to 1000 °C reasonably well.

Since the ideal gases are assumed, the multicomponent diffusive mass flux can be evaluated by using Maxwell–Stefan diffusion coefficients for binary pairs of gas species that are

Table 4 – Molar mass and diffusion volume of gas species [18].

Gas species	Molar mass (g mol ⁻¹)	Diffusion volume (cm ³)
Hydrogen (H ₂)	2	7.07
Oxygen (O ₂)	32	16.6
Nitrogen (N ₂)	28	17.9
Water (H ₂ O)	18	12.7
Carbon dioxide (CO ₂)	44	26.9
Carbon monoxide (CO)	28	18.9
Methane (CH ₄)	16	24.42

dependent on temperature T and total pressure p in the system.

The diffusion coefficient $D_{i,j}$ for a binary mixture of gas species i and j can be estimated by using Fuller, Schettler and Giddings relation [18]:

$$D_{i,j} = \frac{10^{-7} \cdot T^{\frac{7}{4}}}{p \cdot M_{i,j}^{\frac{1}{2}} \cdot (V_i^{\frac{1}{3}} + V_j^{\frac{1}{3}})^2}, \quad (4)$$

$$M_{i,j} = \left(\frac{1}{M_i} + \frac{1}{M_j} \right)^{-1}, \quad (5)$$

where T is the temperature in Kelvin (K), p is the pressure in bar (1 bar = 10⁵ Pa), $M_{i,j}$ is the molar mass in gram per mole (g mol⁻¹) of a gas specie in the binary mixture, and $V_{i,j}$ is the diffusion volume in cubic centimeter (cm³). The values of molar masses and diffusion volumes of all involved gas species are summarized in Table 4 [18].

The boundary conditions are specified as following. The flux of gases is directed along the x-axis with homogeneous mass fractions (Y_i) of gas species and velocity (v) over the entire cross-section area at the fuel/air (anode/cathode) inlet. The inlet mass fractions of gas species in the fuel are:

Table 3 – Physical properties of gas species.

Physical property	Symbol	Value	Unit	Ref.
Hydrogen viscosity	μ_{H_2}	$6.162 \times 10^{-6} + 1.145 \times 10^{-8} \times T$	Pa s	[14]
Oxygen viscosity	μ_{O_2}	$1.668 \times 10^{-5} + 3.108 \times 10^{-8} \times T$	Pa s	[14]
Nitrogen viscosity	μ_{N_2}	$1.435 \times 10^{-5} + 2.642 \times 10^{-8} \times T$	Pa s	[14]
Water viscosity	μ_{H_2O}	$4.567 \times 10^{-6} + 2.209 \times 10^{-8} \times T$	Pa s	[14]
Carbon dioxide viscosity	μ_{CO_2}	$4.743 \times 10^{-6} + 3.429 \times 10^{-8} \times T$	Pa s	[15]
Carbon monoxide viscosity	μ_{CO}	$6.646 \times 10^{-6} + 3.727 \times 10^{-8} \times T$	Pa s	[16]
Methane viscosity	μ_{CH_4}	$4.121 \times 10^{-6} + 2.353 \times 10^{-8} \times T$	Pa s	[15]
Hydrogen thermal conductivity	k_{H_2}	$8.525 \times 10^{-2} + 2.964 \times 10^{-4} \times T$	W m ⁻¹ K ⁻¹	[14]
Oxygen thermal conductivity	k_{O_2}	$1.569 \times 10^{-2} + 5.690 \times 10^{-5} \times T$	W m ⁻¹ K ⁻¹	[14]
Nitrogen thermal conductivity	k_{N_2}	$1.258 \times 10^{-2} + 5.444 \times 10^{-5} \times T$	W m ⁻¹ K ⁻¹	[14]
Water thermal conductivity	k_{H_2O}	$-1.430 \times 10^{-2} + 9.782 \times 10^{-5} \times T$	W m ⁻¹ K ⁻¹	[14]
Carbon dioxide thermal conductivity	k_{CO_2}	$6.750 \times 10^{-3} + 6.460 \times 10^{-5} \times T$	W m ⁻¹ K ⁻¹	[17]
Carbon monoxide thermal conductivity	k_{CO}	$1.505 \times 10^{-2} + 5.660 \times 10^{-5} \times T$	W m ⁻¹ K ⁻¹	[17]
Methane thermal conductivity	k_{CH_4}	$-3.780 \times 10^{-2} + 2.135 \times 10^{-4} \times T$	W m ⁻¹ K ⁻¹	[17]
Hydrogen specific heat	C_{p,H_2}	$1.396 \times 10^4 + 0.950 \times T$	J kg ⁻¹ K ⁻¹	[14]
Oxygen specific heat	C_{p,O_2}	$8.768 \times 10^2 + 0.217 \times T$	J kg ⁻¹ K ⁻¹	[14]
Nitrogen specific heat	C_{p,N_2}	$9.356 \times 10^2 + 0.232 \times T$	J kg ⁻¹ K ⁻¹	[14]
Water specific heat	C_{p,H_2O}	$1.639 \times 10^3 + 0.641 \times T$	J kg ⁻¹ K ⁻¹	[14]
Carbon dioxide specific heat	C_{p,CO_2}	$1.033 \times 10^3 + 0.205 \times T$	J kg ⁻¹ K ⁻¹	[17]
Carbon monoxide specific heat	$C_{p,CO}$	$1.029 \times 10^3 + 0.159 \times T$	J kg ⁻¹ K ⁻¹	[17]
Methane specific heat	C_{p,CH_4}	$2.393 \times 10^3 + 2.182 \times T$	J kg ⁻¹ K ⁻¹	[17]

$Y_{in,i,a} = 0.035, 0.595, 0.055, 0.130, 0.185$, where i is $H_2, H_2O, CO, CO_2, CH_4$. The data from literature indicate that the steam-to-carbon ratio (STCR) must be higher than two to prevent solid carbon deposition within the porous anode and catalyst layer during the methane reforming and shift reactions [19]. Due to this, the inlet mole fraction of steam ($X_{H_2O} = 0.49$) in this model is higher than the sum of two mole fractions of methane ($X_{CH_4} = 0.17$) and carbon monoxide ($X_{CO} = 0.03$). It should be noted that only methane reforming and water-gas-shift reactions are considered in this model as explained in the following section. The inlet mass fractions of gas species in the air are: $Y_{in,i,c} = 0.200, 0.785, 0.015$, where i is O_2, N_2, H_2O . The inlet velocity is denoted with $v_{in,a/c}$ and is equal to 0.5 m s^{-1} and 1.0 m s^{-1} at the anode and cathode side, respectively. The outlet velocity is determined indirectly by defining a constant pressure $p_{ref} = 1.013 \text{ bar}$ of the gas mixture at the outlet. The velocity (v_i) of gas fluxes at the contact walls is determined by no-slip boundary condition that assumes $v_i = 0 \text{ m s}^{-1}$. The modeled symmetry also demands that no flux passes the $z-x$ plane. Furthermore, it is assumed that heat transfer between the porous electrodes/catalyst layers and gases is predominately conductive since the velocity of gas fluxes within the porous electrodes and catalyst layers is low due to dominant diffusive transport of gases through the pores. The same assumption is made for heat transfer between the contact walls and gases due to no-slip boundary condition. Fig. 1b shows the velocity field of gas species in the modeled structure to illustrate and support the assumptions made before. As can be seen, the boundary conditions $v_{in,a} = 0.5 \text{ m s}^{-1}$ and $v_{in,c} = 1.0 \text{ m s}^{-1}$ clearly reflect on the first slice from left side of 3-D plot. The velocity field is then developed across the gas chambers, porous electrodes and catalyst layers. It can be noticed that the velocity is close to zero nearby the contact walls and within the porous electrodes and catalyst layers. The symmetry of velocity about the $z-x$ plane is also obvious.

Porous electrodes

Gas diffusion anode and cathode layers consist of porous media that serve to transport gaseous species to and away from the active reaction sites at the porous electrode/electrolyte interfaces. Beside this, porous electrodes also conduct generated electric current from the reaction sites to the current collectors and contacts with interconnects of the SOFC. The following equations are implemented to model porous electrodes:

- Continuity equation:

$$\vec{\nabla} \cdot (\rho \cdot \vec{v}) = S_m, \quad (6)$$

where ρ is the average density of gas, v is the velocity vector and S_m is the source (or sink) for the production (or consumption) of gas species that can be attributed to electrochemical reactions within the porous electrodes.

- Momentum equation:

The flow of gases in porous media is modeled by the following momentum equation:

$$\frac{\rho}{\epsilon_p} \left((\vec{v} \cdot \vec{\nabla}) \frac{\vec{v}}{\epsilon_p} \right) = \vec{\nabla} \cdot \left[-pI + \frac{\mu}{\epsilon_p} \left((\vec{\nabla} \vec{v}) + (\vec{\nabla} \vec{v})^T \right) - \frac{2\mu}{3\epsilon_p} (\vec{\nabla} \cdot \vec{v}) I \right] - \left(\frac{\mu}{\kappa} + \vec{\nabla} \cdot (\rho \vec{v}) \right) \vec{v}, \quad (7)$$

where μ is viscosity of gases, ϵ_p is porosity and κ is permeability of the electrode media.

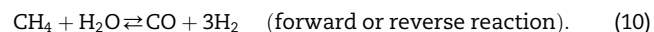
- Species conservation equation:

$$\vec{\nabla} \cdot (\rho \cdot \vec{v} \cdot Y_i) = -\vec{\nabla} \cdot \vec{j}_i + S_i, \quad (8)$$

where j_i is the multicomponent diffusive mass flux vector. Diffusion in porous media is commonly modeled by a molecular (particle-particle collision) and Knudsen (particle-wall collision) diffusion mechanism [20]. However, in this case the diffusivities of gas species in porous media are simplified by using effective diffusion coefficient $D_{i,j,\text{eff}}$. Considering the relation $D_{i,j,\text{eff}} = \epsilon_p^{3/2} \times D_{i,j}$, the j_i is obtained by the following equation:

$$\vec{j}_i = - \sum_{j=1}^{N-1} \rho \cdot D_{i,j,\text{eff}} \cdot \vec{\nabla} Y_j = - \sum_{j=1}^{N-1} \rho \cdot \epsilon_p^{3/2} \cdot D_{i,j} \cdot \vec{\nabla} Y_j, \quad (9)$$

where S_i is the source (or sink) for the production (or consumption) of a gas specie. In this model, the steam reforming of methane and water-gas-shift reactions are considered. As presented by W. Lehnert et al. [7], the methane reforming within the porous anode-cermet is carried out in a two-stage step. The steam reforming of methane is thermodynamically favored at higher temperatures (it is a strongly endothermic reaction) and lower pressures:



The electrochemically active carbon monoxide is converted via water-gas-shift reaction into carbon dioxide and hydrogen:



Since the operational temperatures of the SOFC are from $800^\circ C$ to $1000^\circ C$, it is believed the shift reaction is very quick and remains in equilibrium. The volumetric reaction rate of reforming reaction (10) is expressed as moles of methane reacted per unit volume and time as:

$$R_r = k_r^+ \cdot p_{CH_4} \cdot p_{H_2O} - k_r^- \cdot p_{CO} \cdot (p_{H_2})^3, \quad (12)$$

where k_r^+ and k_r^- are velocity constants of forward and backward steam reforming reactions, p_i is partial pressure of gas specie involved in the reactions. A similar expression is formed for water-gas-shift reaction (11):

$$R_s = k_s^+ \cdot p_{CO} \cdot p_{H_2O} - k_s^- \cdot p_{CO_2} \cdot p_{H_2}, \quad (13)$$

where k_s^+ and k_s^- are velocity constants of forward and backward shift reactions. The values and units of constants are summarized in Table 5 [7].

The molar rates (in $\text{mol m}^{-3} \text{ s}^{-1}$) of formation are expressed as follows:

Table 5 – Velocity constants of forward/backward steam reforming and shift reactions [7].

	T = 1073 K	T = 1123 K	T = 1163 K
k_r^+ (mol m ⁻³ Pa ⁻² s ⁻¹)	2.3×10^{-8}	8.0×10^{-8}	1.6×10^{-7}
k_r^- (mol m ⁻³ Pa ⁻⁴ s ⁻¹)	1.4×10^{-20}	1.5×10^{-20}	1.5×10^{-20}
k_s^+ (mol m ⁻³ Pa ⁻² s ⁻¹)	1.5×10^{-7}	3.2×10^{-7}	3.6×10^{-7}
k_s^- (mol m ⁻³ Pa ⁻² s ⁻¹)	1.4×10^{-7}	3.5×10^{-7}	4.3×10^{-7}

$$R_{CH_4} = -R_r, \quad (14)$$

$$R_{CO} = R_r - R_s, \quad (15)$$

$$R_{H_2O} = -R_r - R_s, \quad (16)$$

$$R_{H_2} = 3 \cdot R_r + R_s, \quad (17)$$

$$R_{CO_2} = R_s. \quad (18)$$

Finally, the mass rates of formation (in kg m⁻³ s⁻¹) are calculated to obtain sources (or sinks) for the production (or consumption) of gas species:

$$S_{CH_4} = M_{CH_4} \cdot R_{CH_4}, \quad (19)$$

$$S_{CO} = M_{CO} \cdot R_{CO}, \quad (20)$$

$$S_{H_2O} = M_{H_2O} \cdot R_{H_2O}, \quad (21)$$

$$S_{H_2} = M_{H_2} \cdot R_{H_2}, \quad (22)$$

$$S_{CO_2} = M_{CO_2} \cdot R_{CO_2}, \quad (23)$$

where M_i is molar mass of gas specie in kg mol⁻¹.

- Charge conservation equation:

The electronic current transport in porous electrodes is modeled by considering conservation of electric charge in a solid metal conductor:

$$\vec{\nabla} \cdot \left(-\sigma_{s,\text{eff}} \cdot \vec{\nabla} \phi_s \right) = 0, \quad (24)$$

where $\sigma_{s,\text{eff}}$ is effective electronic conductivity of porous electrode and ϕ_s is electrostatic potential in the solid phase. It is assumed that no electrical current source is present within the solid metal.

- Energy conservation equation:

The energy transport in porous electrodes is also modeled by considering effective thermal conductivity ($k_{s,\text{eff}}$), and effective product of specific heat (C_p) and specific density (ρ) of the solid material:

$$\vec{\nabla} \cdot \left((\rho \cdot C_p)_{\text{eff}} \cdot \vec{v} \cdot T \right) = \vec{\nabla} \cdot \left(k_{s,\text{eff}} \cdot \vec{\nabla} T \right) + S_e. \quad (25)$$

The values $\sigma_{s,\text{eff}}$, $k_{s,\text{eff}}$, C_p and ρ for porous electrodes are shown in Table 6.

Table 6 – Physical properties of porous electrodes.

Physical property	Symbol	Value	Unit	Ref.
Effective electronic conductivity of porous anode	$\sigma_{sa,\text{eff}}$	4800	S m ⁻¹	[10]
Effective electronic conductivity of porous cathode	$\sigma_{sc,\text{eff}}$	1600	S m ⁻¹	[10]
Effective thermal conductivity of porous anode	$k_{sa,\text{eff}}$	3	W m ⁻¹ K ⁻¹	[10]
Effective thermal conductivity of porous cathode	$k_{sc,\text{eff}}$	2	W m ⁻¹ K ⁻¹	[10]
Anode material specific heat	$C_{p,a}$	595	J kg ⁻¹ K ⁻¹	[10]
Cathode material specific heat	$C_{p,c}$	573	J kg ⁻¹ K ⁻¹	[10]
Anode material specific density	ρ_a	6870	kg m ⁻³	[10]
Cathode material specific density	ρ_c	6570	kg m ⁻³	[10]

The source/sink term S_e is evaluated by considering ohmic heating that is modeled as:

$$S_e = \sigma_{s,\text{eff}} \cdot \vec{\nabla} \phi_s \cdot \vec{\nabla} \phi_s. \quad (26)$$

Appropriate boundary conditions have to be applied to the porous electrodes as well. At the left and right side of the calculation domain the symmetry condition for electrostatic potential in the solid phase, velocity, mass and heat fluxes is applied at the anode and cathode side. The interfaces between the porous electrodes and contact/catalyst layers are modeled with continuity of electric current density and heat flux through the interface.

At the front (at the fuel/air inlet) and at the back (at the fuel/air outlet) side of the SOFC the insulation of the electric current, i.e. the current density through the surface is assumed zero, is applied. The same is valid for velocity and mass flux of gas species.

Catalyst layers

The implemented equation for modeling the electronic current transport in catalyst layers is similar to the Equation (24), with exception the source/sink terms S_s are added on its right hand side and $\sigma_{s,\text{eff}}$ has to be corrected to account for mixed ionic and electronic conductivity. An additional charge conservation equation is added for ionic charge transfer that is used to calculate the ionic current transport:

$$\vec{\nabla} \cdot \left(-\sigma_{el,\text{eff}} \cdot \vec{\nabla} \phi_{el} \right) = A_s \cdot S_{el}, \quad (27)$$

where $\sigma_{el,\text{eff}}$ is effective ionic conductivity of the catalyst layer, ϕ_{el} is electrolyte potential, the A_s is the active surface area per unit volume, and the source/sink term S_{el} represents the ionic current density.

Furthermore, the current density has to be coupled with source/sink terms in the mass and species conservation equations. At the interface between the anode porous electrode and catalyst layer the fuel (hydrogen or carbon monoxide) is consumed and the water or carbon dioxide is produced, so the sink terms are (28), (29) and the source terms are (30), (31):

$$S_{H_2} = -\frac{M_{H_2} \cdot i_{a,H_2}}{2 \cdot F}, \quad (28)$$

$$S_{CO} = -\frac{M_{CO} \cdot i_{a,CO}}{2 \cdot F}, \quad (29)$$

$$S_{H_2O} = +\frac{M_{H_2O} \cdot i_{a,H_2}}{2 \cdot F}, \quad (30)$$

$$S_{CO_2} = +\frac{M_{CO_2} \cdot i_{a,CO}}{2 \cdot F}. \quad (31)$$

At the interface between the cathode porous electrode and catalyst layer, the oxygen is consumed, so the sink term is:

$$S_{O_2} = -\frac{M_{O_2} \cdot i_{c,O_2}}{2 \cdot F}, \quad (32)$$

where the $i_{a/c}$ is anodic/cathodic current density source and $F = 96457 \text{ As mol}^{-1}$ is Faraday constant. Furthermore, when evaluating the source/sink terms in the charge conservation Equations (24) and (27), the electronic current density is a sink term in the anode/cathode catalyst layer:

$$S_s = -i_{a/c}, \quad (33)$$

and the ionic current density is a source term in the anode/cathode catalyst layer:

$$S_{el} = +i_{a/c}. \quad (34)$$

The anodic and cathodic current density $i_{a/c}$ is defined by Butler–Volmer equation [21]:

$$i_{a/c} = i_{0,a/c} \cdot \left[e^{\left(\frac{a^{a/c} \cdot z \cdot F \cdot \eta_{act,a/c}}{R \cdot T} \right)} - e^{\left(\frac{a^{a/c} \cdot z \cdot F \cdot \eta_{act,c}}{R \cdot T} \right)} \right]. \quad (35)$$

The anodic exchange current density $i_{0,a}$ can be formulated as a sum of exchange current densities, each one defining one oxidation process, namely H_2 – H_2O and CO – CO_2 oxidation, in this specific case [21]:

$$i_{0,a}^{H_2} = i_{H_2} \cdot \left[\frac{\left(\frac{p_{H_2}}{p_{ref}} \right)^{\frac{1}{4}} \cdot \left(p_{H_2O} \right)^{\frac{3}{4}}}{1 + \left(\frac{p_{H_2}}{p_{ref}} \right)^{\frac{1}{2}}} \right], \quad (36)$$

$$i_{0,a}^{CO} = i_{CO} \cdot \left[\frac{\left(\frac{p_{CO}}{p_{ref}} \right)^{\frac{1}{4}} \cdot \left(p_{CO_2} \right)^{\frac{3}{4}}}{1 + \left(\frac{p_{CO}}{p_{ref}} \right)^{\frac{1}{2}}} \right], \quad (37)$$

$$i_{0,a} = i_{0,a}^{H_2} + i_{0,a}^{CO}, \quad (38)$$

where p_i is partial pressure of a gas specie and p_{ref} is reference pressure. The latter is equal to 1.013 bar in this study. The i_{H_2} and i_{CO} are empirical constants that can be used for fitting the simulation results with experimental data. It was found that the rate of CO – CO_2 oxidation is about 2–3 times lower than the rate of H_2 – H_2O oxidation [21], so the i_{CO} is adjusted to approximately one third of i_{H_2} . The cathodic exchange current density $i_{0,c}$ can be formulated in a similar way as following:

$$i_{0,c} = i_{0,c}^{O_2} = i_{O_2} \cdot \left[\frac{\left(\frac{p_{O_2}}{p_{ref}} \right)^{\frac{1}{4}}}{1 + \left(\frac{p_{O_2}}{p_{ref}} \right)^{\frac{1}{2}}} \right]. \quad (39)$$

Table 7 summarizes the parameters used as inputs for modeling the anode/cathode exchange current density in the catalyst layers, including their values, units and references. Please note that constant values of the exchange current densities are used.

The anode activation overpotential $\eta_{act,a}$ is calculated as a difference between the solid phase and electrolyte phase electrostatic potential of the anode catalyst layer:

$$\eta_{act,a} = \phi_{s,a} - \phi_{el,a}, \quad (40)$$

and the cathode activation overpotential $\eta_{act,c}$ is calculated similarly:

$$\eta_{act,c} = \phi_{s,c} - \phi_{el,c} - V_{oc}, \quad (41)$$

where the solid phase and electrolyte phase electrostatic potentials in the anode catalyst layer are denoted with $\phi_{s,a}$ and $\phi_{el,a}$, whereas the solid phase and electrolyte phase electrostatic potentials in the cathode catalyst layer are denoted with $\phi_{s,c}$ and $\phi_{el,c}$. The V_{oc} is the open circuit voltage of the SOFC that can be calculated by evaluating Nernst equation:

$$V_{oc} = V^0 + \frac{R \cdot T}{4 \cdot F} \cdot \ln \left[p_{O_2} \cdot \left(\frac{p_{H_2}}{p_{H_2O}} \right)^2 \right]. \quad (42)$$

For simplicity, a constant value of $V_{oc} = 0.95 \text{ V}$ is used as model input in this case.

The energy transport equation is similar to the Equation (25), with exception the heat source term S_e has to be adjusted according the chemical, electrochemical and ohmic heat generation. The reversible heat is generated in the anode

Table 7 – Properties of catalyst layers.

Property	Symbol	Value	Unit	Ref.
Active surface area	A_s	1.025×10^5	m^{-1}	[22]
Anodic exchange current density, H_2 – H_2O	$i_{0,a}^{H_2}$	5.3×10^3	A m^{-2}	[20]
Anodic exchange current density, CO – CO_2	$i_{0,a}^{CO}$	1.7×10^3	A m^{-2}	[21]
Anodic exchange current density, sum	$i_{0,a}$	7.0×10^3	A m^{-2}	[20,21]
Cathodic exchange current density	$i_{0,c}$	2.0×10^3	A m^{-2}	[20]
Anodic charge transfer coefficient, anode	α_a^a	2	/	[23]
Cathodic charge transfer coefficient, anode	α_c^a	1	/	[23]
Anodic charge transfer coefficient, cathode	α_a^c	1.5	/	[23]
Cathodic charge transfer coefficient, cathode	α_c^c	0.5	/	[23]
Effective anode ionic conductivity	$\sigma_{ea,eff}$	0.29	S m^{-1}	[23]
Effective cathode ionic conductivity	$\sigma_{ec,eff}$	0.24	S m^{-1}	[23]

catalyst layer due to chemical reaction as the fuel is oxidized. The reversible heat term $q_{\text{rev,a}}$ is calculated as:

$$q_{\text{rev,a}} = -\frac{i_a \cdot \Delta H_{\text{fuel}}}{2 \cdot F}, \quad (43)$$

where i_a is anodic current density and ΔH_{fuel} is the standard enthalpy change of formation. The $\Delta H_{\text{H}_2} = -241 \text{ kJ mol}^{-1}$ and $\Delta H_{\text{CO}} = -283 \text{ kJ mol}^{-1}$ are taken from Ref. [7] and assumed constant since no reliable data regarding their temperature dependence was found.

Since the rate of hydrogen oxidation is assumed three times faster than that of carbon monoxide, the $\Delta H_{\text{fuel}} = \frac{3}{4} \cdot \Delta H_{\text{H}_2} + \frac{1}{4} \cdot \Delta H_{\text{CO}} = -251.5 \text{ kJ mol}^{-1}$.

The irreversible heat generation in the anode is attributed to electrochemical reaction that occurs when the charge is transferred from the electrolyte (ionic) to the solid (electronic) phase. The irreversible heat term $q_{\text{irr,a}}$ is calculated as:

$$q_{\text{irr,a}} = i_{\text{a,eff}} \cdot \eta_{\text{act,a}}. \quad (44)$$

The ohmic heat term $q_{\text{ohm,a}}$ is calculated as:

$$q_{\text{ohm,a}} = \sigma_{\text{sa,eff}} \cdot \vec{\nabla} \phi_s \cdot \vec{\nabla} \phi_s + \sigma_{\text{ea,eff}} \cdot \vec{\nabla} \phi_{\text{el}} \cdot \vec{\nabla} \phi_{\text{el}}, \quad (45)$$

where the $\sigma_{\text{sa,eff}}$ and $\sigma_{\text{ea,eff}}$ are effective anode electronic and ionic conductivity. The total heat generation term $S_{\text{e,a}}$ is the sum of $q_{\text{rev,a}}$, $q_{\text{irr,a}}$ and $q_{\text{ohm,a}}$:

$$S_{\text{e,a}} = q_{\text{rev,a}} + q_{\text{irr,a}} + q_{\text{ohm,a}}. \quad (46)$$

The irreversible heat term $q_{\text{irr,c}}$ in the cathode is calculated similarly:

$$q_{\text{irr,c}} = i_{\text{c,eff}} \cdot \eta_{\text{act,c}}. \quad (47)$$

The ohmic heat term $q_{\text{ohm,c}}$ is calculated as:

$$q_{\text{ohm,c}} = \sigma_{\text{sc,eff}} \cdot \vec{\nabla} \phi_s \cdot \vec{\nabla} \phi_s + \sigma_{\text{ec,eff}} \cdot \vec{\nabla} \phi_{\text{el}} \cdot \vec{\nabla} \phi_{\text{el}}, \quad (48)$$

where the $\sigma_{\text{sc,eff}}$ and $\sigma_{\text{ec,eff}}$ are effective cathode electronic and ionic conductivity. The total heat generation term $S_{\text{e,c}}$ is the sum of $q_{\text{irr,c}}$ and $q_{\text{ohm,c}}$:

$$S_{\text{e,c}} = q_{\text{irr,c}} + q_{\text{ohm,c}}. \quad (49)$$

At the left and right side of the anode and cathode catalyst layer the symmetry condition for electrostatic potential in the solid and electrolyte phase, velocity, mass and heat flux is applied, respectively. The interfaces between the catalyst layers and electrolyte/porous electrodes are modeled with continuity of the electric current density and heat flux through these interfaces. The interfaces between the catalyst layers and porous electrodes are also modeled with continuity of velocity and mass flux.

Oppositely, at the interfaces between the catalyst layers and electrolyte, the gas species are not allowed to pass into the electrolyte layer due to its dense (non-porous) structure, so the normal components of velocity and mass flux vectors at these boundaries are zero. At the front (at the fuel/air inlet) and at the back (at the fuel/air outlet) side of the SOFC the insulation of the electric current, i.e. the current density through the surface is assumed zero, is applied. The same is valid for velocity and mass flux of gas species.

Electrolyte

The charge conservation equation is applied to dense electrolyte in the following form:

$$\vec{\nabla} \cdot \left(-\sigma_{\text{el}} \cdot \vec{\nabla} \phi_{\text{el}} \right) = 0. \quad (50)$$

Right hand side of Equation (50) is zero since there is no current source within the electrolyte. Only the transport of oxygen ions is considered here for simplicity. The heat transfer through the electrolyte layer is modeled by the following equation:

$$\vec{\nabla} \cdot \left(k_{\text{el}} \cdot \vec{\nabla} T \right) + \sigma_{\text{el}} \cdot \vec{\nabla} \phi_{\text{el}} \cdot \vec{\nabla} \phi_{\text{el}} = 0, \quad (51)$$

where the k_{el} is specific thermal conductivity and σ_{el} is specific ionic conductivity of dense electrolyte. The heat source is attributed to losses due to ionic charge transfer through the electrolyte with finite σ_{el} .

As mentioned before, due to non-porous structure of electrolyte, this layer is impermeable to gases. Thus, the velocity and mass flux components normal to the electrolyte surface are zero. The continuity boundary condition for ionic current density and heat flux is applied at the interfaces between the electrolyte and catalyst layers (anode and cathode). Other surfaces of the electrolyte are insulated to ionic current density by setting its normal component to zero.

Contacts with interconnects

The metallic contacts with interconnects allow the current collection and transport to external electric (ohmic) load that is powered by the SOFC. The modeled contacts with interconnects also form gas chambers of the SOFC. The charge conservation equation is used to model electric current density within the contact layers:

$$\vec{\nabla} \cdot \left(-\sigma_m \cdot \vec{\nabla} \phi_s \right) = 0, \quad (52)$$

where σ_m represents conductivity of the metal. Obviously, there is no current sources or sinks within the modeled contacts.

Furthermore, energy conservation equation is used to model ohmic heating within the contacts:

$$\vec{\nabla} \cdot \left(k_m \cdot \vec{\nabla} T \right) + \sigma_m \cdot \vec{\nabla} \phi_s \cdot \vec{\nabla} \phi_s = 0. \quad (53)$$

It is assumed that Crofer® 22H [24] high-temperature ferritic stainless steel for SOFC applications is used as interconnect material. The thermal conductivity k_m is about $26 \text{ W m}^{-1} \text{ K}^{-1}$ and specific electric conductivity σ_m is about $9 \times 10^5 \text{ S m}^{-1}$ at $T = 800 \text{ }^\circ\text{C}$.

The boundary conditions for constant electrostatic potential (ϕ_s) are applied on the top (cathode) and bottom (anode) interconnect surface of the SOFC:

$$\phi_{s,c} = V_{\text{cell}}, \quad (54)$$

$$\phi_{s,a} = 0. \quad (55)$$

The continuity of electric current density and heat flux is applied at the interfaces between the contacts and porous

electrodes. It should be pointed out that convective heat transfer is not allowed due to applied no-slip boundary condition for velocity of gases inside the chambers. Only the conductive heat transfer between the contacts/interconnects and gases is allowed. The radiative heat transfer boundary condition is added on the top, bottom, front and backside of the modeled SOFC structure when the influence of thermal radiation is studied:

$$P_{\text{rad}} = \varepsilon \cdot \sigma \cdot (T^4 - T_{\text{amb}}^4), \quad (56)$$

where P_{rad} is radiative power density (in W m^{-2}), ε is emissivity constant (between 0 and 1), σ is Stefan constant ($5.67 \times 10^{-8} \text{ W m}^{-2} \text{ K}^{-4}$), T is temperature at the surface, T_{amb} is ambient temperature.

Results and discussion

The 3-D modeling of SOFC described in the previous sections is continued with simulation results with some discussions.

Fig. 2 shows the calculated current/power density (J/P) characteristic as a function of SOFC's output voltage. The J/P characteristic in **Fig. 2** is compared to that in **Fig. 5**, presented by P. Aguiar et al. [6]. Similar values ($J = 8934 \text{ A m}^{-2}$ at $V_{\text{cell}} = 0.5 \text{ V}$, or $P_{\text{mp}} = 4521 \text{ W m}^{-2}$, **Fig. 2**) can be noticed (approximately $J = 8500 \text{ A m}^{-2}$ at $V_{\text{cell}} = 0.5 \text{ V}$, or $P_{\text{mp}} = 4400 \text{ W m}^{-2}$ at $T = 1073 \text{ K}$ and $U_f = 0.85$, **Fig. 5** [6]). Moreover, the results presented by H. Zhu et al. [25] also show that the methane-fueled SOFC can generate maximum power density $P_{\text{mp}} = 3200\text{--}4200 \text{ W m}^{-2}$ if operating voltage V_{cell} is set to about 0.5 V and the current density $J = 6000\text{--}8000 \text{ A m}^{-2}$.

The J/P characteristic can be very useful when SOFC operates as electric generator and as much as possible power needs to be extracted. The maximum power point (P_{mp}) can be predicted from simulation results when the scan over the output cell's voltages (V_{cell}) is performed. As can be seen in **Fig. 2**, the P_{mp} occurs when V_{cell} is 0.55 V. This indicates that the output power density (P) decreases if the V_{cell} is below 0.55 V, regardless the current density (J) increases. The latter is

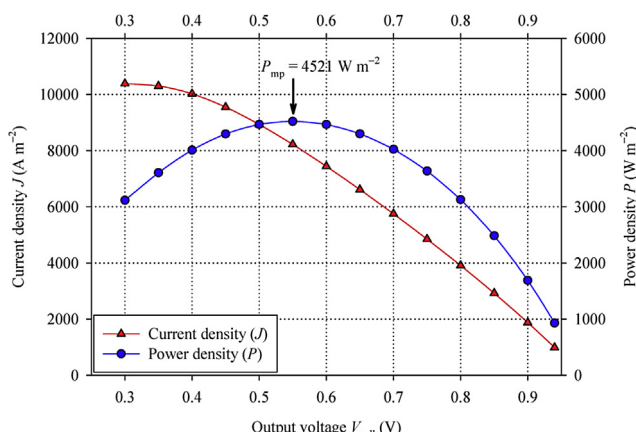


Fig. 2 – Current (J) and power (P) density of the modeled solid oxide fuel cell (SOFC) as a function of output voltage (V_{cell}). The maximum power density (P_{mp}) is reached at $V_{\text{cell}} = 0.55 \text{ V}$.

also dangerous since the generated power is thermally dissipated within the SOFC structure (mainly within the electrolyte and catalyst layers due to the high potential drop, but also within porous electrode layers and contacts) and the temperature T of the SOFC can potentially exceed the maximum operating temperature that is about 1000 °C [3]. This can lead to degradation or, finally, to failure of a realistic SOFC.

Fig. 3a shows surface temperature distribution of the modeled SOFC structure at maximum power point P_{mp} . It can be noticed that the temperature gradually increases from the air/fuel inlet side towards the middle of the structure since the heat exchange between the SOFC structure and its surroundings is allowed by the air/fuel flow through the chambers. In other words, the flow of air/fuel carries away the heat, i.e. ohmic (due to electric current), reversible and irreversible (due to chemical and electrochemical reactions), generated within the structure. The temperature slightly decreases from the middle towards the air/fuel outlet side since the heat is also exchanged through the surface by the thermal radiation. It is assumed that emissivity constant ε is equal to 0.8.

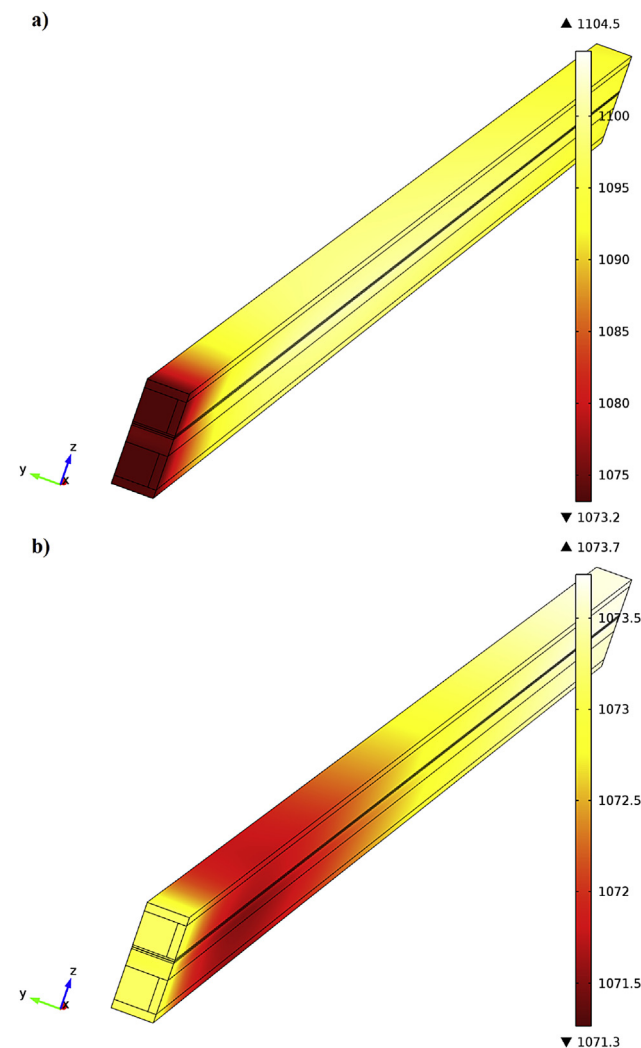


Fig. 3 – Surface temperature (in Kelvin) of the modeled solid oxide fuel cell (SOFC) a) at maximum power point ($P_{\text{mp}} = 4521 \text{ W m}^{-2}$) and b) at low output power ($P = 930 \text{ W m}^{-2}$).

However, it should be pointed out that the temperature inside the SOFC can also drop below the temperature of inlet gases or/and the temperature of ambient, especially at low current (power) densities, as shown in Fig. 3b, due to internal methane reforming reactions. The methane reforming is endothermic reaction that consumes the heat, thus the temperature is locally lowered. Fig. 4 shows a) temperature T , reforming and shift reaction rate $R_{r/s}$, and b) mole fractions X_i of gas species along the x-axis at the interface between the porous anode and anode catalyst layer. It can be observed that the temperature close to the fuel inlet (at $x = 0$ mm) is lowered, since the reforming reaction rate is high due to high mole concentration of methane. As the methane is gradually consumed along the fuel channel, the reforming reaction rate decreases, and the temperature increases. However, if the current (power) density is higher, the locally produced heat is higher than consumed by reforming reaction, and the temperature is higher than the ambient temperature of 1073 K elsewhere within the modeled SOFC structure, similarly as seen in Fig. 3a.

Please note that R_i should be calculated by inserting the $R_{r/s}$ into the Equations (14)–(18). The lower absolute values of R_i in this case are possibly attributed to lower temperature (1073 K in this study versus 1123 K in Ref. [7]) that influences the k_r^+ . The k_r^+ is about three times lower (as can be seen in Table 5) and, considering Equation (12), the calculated R_i is lower.

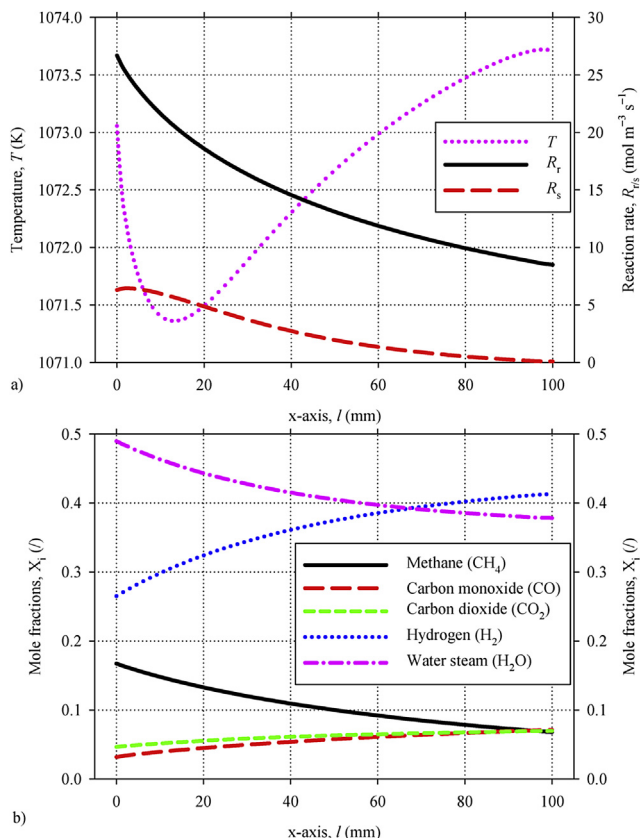


Fig. 4 – a) Temperature T , reforming/shift reaction rate $R_{r/s}$, and b) mole fractions X_i of gas species along the x-axis at the interface between the porous anode and anode catalyst layer of the modeled solid oxide fuel cell (SOFC).

From the results, it can be concluded that the reforming and shift reactions influence the temperature distribution within the modeled SOFC structure.

The main goal of the following test is to verify if the reaction rate model is consistent and reproduces comparable results to those from literature. A similar operating conditions to those in Ref. [7] are set in the following simulation to verify if the molar rates of formation match closely: the ambient temperature (T_{amb}) is 1123 K (850 °C), the thickness of anode support layer (d_s) is 2 mm, the current density J is about 0.3 A cm^{-2} . The other input parameters are the same as those in previous calculations. Fig. 5 shows the temperature T and molar rates R_i of formation for all gas species within the porous anode support layer as a function of z-axis at the fuel inlet ($x = 0$ mm) of the modeled SOFC. The $R_i = -70.98, +65.27, +5.71, +218.65$, and $-76.69 \text{ mol m}^{-3} \text{s}^{-1}$ for $i = \text{CH}_4, \text{CO}, \text{CO}_2, \text{H}_2$, and H_2O , respectively, at the interface between the anode gas chamber and anode support layer (at $d_s = 0$ mm). These values are similar to those presented in Ref. [7], but the profiles of R_i along the z-axis differ, probably due to mismatch between the models (3-D model in this study vs. 1-D model in Ref. [7]) and differences between some of the input parameters. It can be seen the minimum temperature ($T_{\text{min}} = 1120 \text{ K}$) is reached close to the middle of the anode support layer (at $d_s = 0.92 \text{ mm}$). This local minimum at $x = 0 \text{ mm}$ (global minimum is at $0 \text{ mm} < x < 20 \text{ mm}$ as already seen in Fig. 4a) is expected since the methane reforming is endothermic reaction that consumes the heat. The T is locally lowered to the level that establishes sufficient temperature gradient for heat transfer according to the boundary conditions (the inlet temperature is bounded at 1123 K) and effective thermal conductivity of porous anode ($k_{\text{sa,eff}} = 3 \text{ W m}^{-1} \text{ K}^{-1}$). The local minimum of temperature gradient $\Delta T/\Delta z_{\text{min}} = -10,000 \text{ K m}^{-1}$ ($\Delta T/\Delta x_{\text{min}} = -3500 \text{ K m}^{-1}$) is observed at $d_s = 0 \text{ mm}$, whereas the $\Delta T/\Delta z_{\text{max}}$ of about $+6400 \text{ K m}^{-1}$ and $+7800 \text{ K m}^{-1}$ are observed within the porous anode catalyst layer and electrolyte layer. These high temperature gradients are critical since

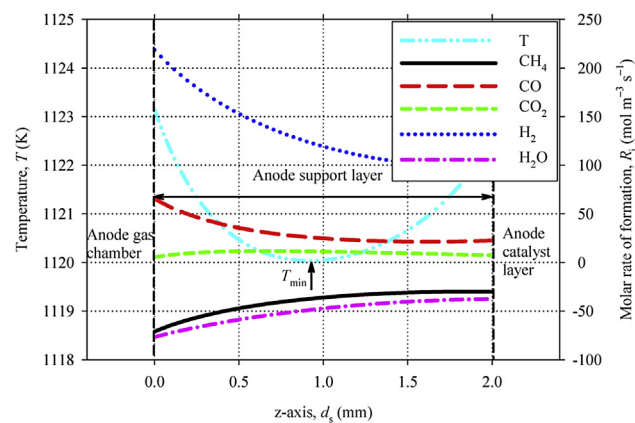


Fig. 5 – Temperature (T) and molar rates (R_i) of formation for gas species within the porous anode support layer as a function of z-axis at the fuel inlet of the modeled solid oxide fuel cell (SOFC). The ambient temperature (T_{amb}) is 1123 K (850 °C), the pressure (p_{ref}) is 1.013 bar, the output current density (J) is about 0.3 A cm^{-2} at cell's voltage $V_{\text{cell}} = 0.85 \text{ V}$.

the coefficient of thermal expansion (CTE) mismatch between the porous anode and the electrolyte layer has been widely reported to be the main cause of thermomechanical failure of SOFCs [26].

Moreover, thermal stresses at the interface between the ceramic sealant and metallic interconnect in planar SOFC stacks may cause failure of sealing with excessive deformation, leading to gas leakage and electrochemical performance degradation [27]. However, it can be concluded that the SOFC model including the steam reforming and shift reactions makes sense since the simulation results give more accurate spatial distributions of temperature and its gradients.

The thermal radiation, which is included with Equation (56) in SOFC model A, is disabled at the top, bottom, front and backside of the calculation domain, if considering SOFC model B. The radiative heat flux is zero at the left and right side by default since a symmetric calculation domain within the modeled structure is chosen.

Fig. 6 shows a) the temperature profiles and b) temperature gradients along the x-axis at the interface between the porous anode and anode catalyst layer at different SOFC's output voltages V_{cell} , considering model A with, and model B without thermal radiation. The differences between the temperature profiles obtained from the model B and model A increase with

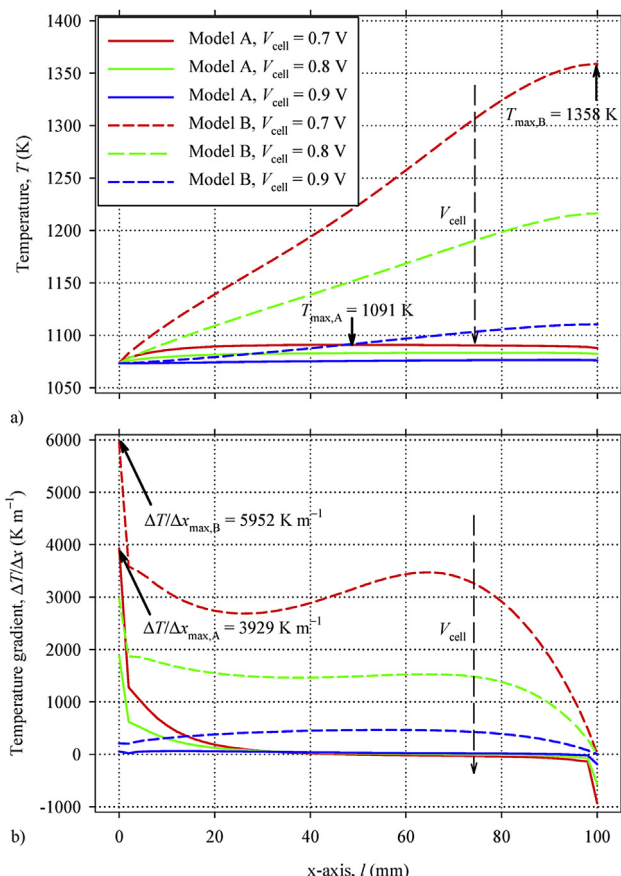


Fig. 6 – a) Temperature profiles and b) temperature gradients along the x-axis at the interface between the porous anode and anode catalyst layer considering SOFC model A with, and model B without thermal radiation. The output voltage V_{cell} is varied from 0.7 V to 0.9 V.

increasing (decreasing) the J (V_{cell}) due to increased heat generation since a higher temperature within the structure is needed to achieve thermal equilibrium with surroundings when using the model B instead of model A. It can be seen in **Fig. 6a** the difference between the temperature distributions within the calculation domain of the model B and model A can be very high ($\Delta T = 270$ K at $l = 100$ mm, $V_{\text{cell}} = 0.7$ V). Similar difference is obtained if the maximum temperatures along the x-axis are compared ($T_{\text{max},B} = 1358$ K vs. $T_{\text{max},A} = 1091$ K). Moreover, it can be noticed that the $T_{\text{max},B} = 1085$ °C critically exceeds the maximum operating temperature of a realistic SOFC, if it is supposed to be about 1000 °C. Since the input parameters in **Tables 3 and 5**, the diffusion coefficients $D_{i,j}$ in Equation (4), the anodic/cathodic current density $i_{a/c}$ in Equation (35), etc., are temperature dependent, the SOFC model B may also produce inaccurate results and might be inappropriate for high-temperature operating conditions. For example, the current density of the SOFC, considering model A, $J_A = 1878, 3909, 5749 \text{ A m}^{-2}$, whereas the current density, considering model B, $J_B = 1860, 3769, 5346 \text{ A m}^{-2}$ at $V_{\text{cell}} = 0.9, 0.8, 0.7$ V, respectively. As can be noticed, the relative difference between the current density J_A and J_B is approximately 1%, 4%, 8%, and increases with decreasing the V_{cell} . It can be seen in **Fig. 6b** that the maximum temperature gradients ($\Delta T / \Delta x_{\text{max},A/B}$) of the modeled SOFC occur at the fuel inlet ($l = 0$ mm, $V_{\text{cell}} = 0.7$ V). The $\Delta T / \Delta x_{\text{max},B}$ is about 50% higher than $\Delta T / \Delta x_{\text{max},A}$, which means that the calculated maximum temperature gradients might be overestimated if using model B instead of model A.

Furthermore, by considering high operating temperature of a realistic SOFC, which ranges from 800 °C to 1000 °C, it is reasonable to model radiative heat transfer to the surroundings, since the local radiated heat, e.g. $P_{\text{rad}} = 4137 \text{ W m}^{-2}$ at $\epsilon = 0.8$, $T_{\text{max},A} = 1091$ K and $T_{\text{amb}} = 1073$ K, is high. Please note that the local radiated heat P_{rad} is also comparable with output power density ($P = 4024 \text{ W m}^{-2}$ at $V_{\text{cell}} = 0.7$ V, **Fig. 2**) of the SOFC, and it should not be neglected.

Similar conclusions have been made by L. Petrucci et al. [5]. The main difference (beside some differences between models and fuel compositions) is that the co-flow configuration of the SOFC is used in this study, whereas the cross-flow configuration is used in Ref. [5]. However, the electrical power ($P = 3127 \text{ W m}^{-2}$ at $V_{\text{cell}} = 0.8$ V and temperature about 800 °C, **Fig. 2**) of the modeled SOFC is similar to the electrical power ($P = 3200 \text{ W m}^{-2}$ at $V_{\text{cell}} = 0.8$ V and temperature about 800 °C), which is reported in Ref. [5].

The temperature profiles in **Fig. 6a**, obtained by using SOFC model A, are also similar to the temperature profiles at fixed distance from air inlet, as can be seen in Fig. 12, presented in Ref. [5]. The comparison is reasonable since the inlet velocity $v_{\text{in},c} = 1.0 \text{ m s}^{-1}$ of air provides sufficient mass fraction of oxygen along the cathode chamber in this case (in co-flow configuration) and insignificantly influences the output current density J and total heat generation, so it is assumed that different configuration is irrelevant.

For example, the difference between the maximum and minimum temperature ΔT is 10–20 °C and the maximum temperature T_{max} is observed approximately in the middle of the SOFC in both cases. The values of temperatures are also similar, which implies that the results in this study are in

accordance with the results, which were presented by the other researchers [5]. Due to these arguments, the SOFC model A is used in the following.

When a realistic SOFC operates as an electric current generator, it is also important to be controlled in such way to achieve the desired output power and to utilize the inlet mixture of fuel gases (hydrogen, carbon monoxide and methane for this case) as much as possible. In other words, the ratio between the outlet and inlet mole fraction of a fuel gas should be as low as possible. The fuel utilization (U_f) may be controlled by adjusting the inlet velocity and composition of gas mixture [28]. However, it is crucial that the maximum temperature and temperature gradient within the SOFC are not exceeded during the operation. In the following, the optimum operating point of the SOFC is studied in terms of chemical-to-electrical conversion efficiency (η_e) combined with U_f . The η_e is formulated with:

$$\eta_e = \frac{P_{el,out}}{P_{ch,in}} = \frac{2 \cdot F \cdot I_{cell} \cdot V_{cell}}{\iiint_{Anode} \Delta H_{fuel} \cdot i_{reac} \cdot dx \cdot dy \cdot dz}, \quad (57)$$

where the $P_{el,out}$ is output electrical power (product of current I_{cell} and voltage V_{cell}) dissipated on SOFC's load, $P_{ch,in}$ is input power that is proportional to the standard enthalpy change and rate of the chemical reactions (oxidation of hydrogen and carbon monoxide) within the anode active layer. The i_{reac} is reaction current density (in $A m^{-3}$) that has to be integrated over the volume of anode active layer. In this case, solely the chemical-to-electrical conversion efficiency is considered. The overall conversion efficiency of a SOFC can be formulated in a different way when the efficiency of whole power plant (including gas turbines, reactors, heaters and inverters) is considered [29]. The U_f is formulated with:

$$U_f = 1 - \frac{4 \cdot \dot{n}_{CH_4,out} + \dot{n}_{H_2,out} + \dot{n}_{CO,out}}{4 \cdot \dot{n}_{CH_4,in} + \dot{n}_{H_2,in} + \dot{n}_{CO,in}}, \quad (58)$$

where the $\dot{n}_{f,in}$ and $\dot{n}_{f,out}$ are the total molar fluxes (in mole per second) of fuel gas species at the fuel inlet and outlet side. The multiplying factor of four is applied since one mole of methane (with one mole of water steam) produces three moles of hydrogen and one mole of carbon monoxide during the steam reforming reaction, Equation (10).

It should be noted that U_f is applied to gas species that are directly (oxidation of hydrogen and carbon monoxide) and indirectly (steam reforming reaction of methane produces hydrogen and carbon monoxide) involved in electrochemical reactions.

Fig. 7a–d shows the power density (P), fuel utilization (U_f), electrical (η_e) and total conversion efficiency ($\eta_{tot} = U_f \times \eta_e$) of the modeled SOFC as a function of output current density (J) and velocity of fuel gas ($v_{in,a}$) at the anode inlet. The J ranges from 1000 to 10,000 $A m^{-2}$, which is a common value of J for realistic SOFC under operation [3]. The $v_{in,a}$ is varied from 0.2 $m s^{-1}$ to 1.0 $m s^{-1}$ by increments of 0.1 $m s^{-1}$ to study P , U_f , η_e , η_{tot} . As can be seen in these plots, the maximum power density (P_{mp}), fuel utilization ($U_{f,max}$), electrical ($\eta_{e,max}$) and total conversion efficiency ($\eta_{tot,max}$) are not coincident. It can be noticed that the P_{mp} occurs at lower J (around 8000 $A m^{-2}$) than $U_{f,max}$ or $\eta_{tot,max}$, which means the J must be higher than the J at P_{mp} to achieve $U_{f,max}$ or $\eta_{tot,max}$. The latter is

undesirable in terms of increasing the temperature and temperature gradients within the structure, as discussed previously. However, if the excessive heat is recycled by other components of the power plant (e.g. reactors or steam turbines), this could be beneficial in terms of increasing the overall conversion efficiency. It can be also noticed that increasing the $v_{in,a}$ from 0.3 $m s^{-1}$ to 1.0 $m s^{-1}$ is inefficient since the U_f (at $P_{mp} = 4500 W m^{-2}$, $J = 8200 A m^{-2}$, $V_{cell} = 0.55 V$) drops from around 0.68 to only 0.11, whereas the P of the SOFC is just slightly increased (by 0.1% relatively). The η_e drops with increasing the J (from 0.72 at 1000 $A m^{-2}$ to 0.31 at 10,000 $A m^{-2}$) and is almost independent on the variation of the $v_{in,a}$ from 0.3 $m s^{-1}$ to 1.0 $m s^{-1}$. The η_{tot} drops with increasing the $v_{in,a}$ (from 28.5% at $v_{in,a} = 0.3 m s^{-1}$ and $J = 8200 A m^{-2}$ to 4.5% at $v_{in,a} = 1.0 m s^{-1}$ and $J = 8200 A m^{-2}$) or/and decreasing the J (from 28.5% at $J = 8200 A m^{-2}$ and $v_{in,a} = 0.3 m s^{-1}$ to 1.4%/0.3% at $J = 1000 A m^{-2}$ and $v_{in,a} = 0.3 m s^{-1}/1.0 m s^{-1}$).

Please note that the results for $v_{in,a} < 0.2 m s^{-1}$ are not shown in graphs since J saturates at lower value than 8200 $A m^{-2}$, since almost all fuel gas is used ($U_f = 1$ if all fuel gas was used).

The $P_{mp} = 4500 W m^{-2}$ also cannot be reached if almost all fuel gas is used. In this case, the power density P drops abruptly since the anode concentration overpotential becomes so large that no fuel can reach the anode TPBs [25]. Moreover, the operating conditions at $U_f = 1$ are undesirable due to degradation processes that might occur when the local fuel starvation and the anode reoxidation within a realistic SOFC are present [30].

It can be concluded that $0.3 m s^{-1} < v_{in,a} < 1.0 m s^{-1}$ results in lower U_f and η_{tot} , whereas $0 m s^{-1} < v_{in,a} < 0.2 m s^{-1}$ results in lower P_{mp} . The SOFC should operate around its P_{mp} ($J = 8000 A m^{-2}$), while the $v_{in,a}$ needs to be properly controlled ($0.2 m s^{-1} < v_{in,a} < 0.3 m s^{-1}$) to achieve high P_{mp} , U_f , η_e and η_{tot} . These results are very important when designing control for realistic SOFC since they show the guideline for setting appropriate inlet velocity of fuel gas ($v_{in,a}$). As can be seen, the $v_{in,a} = 0.3 m s^{-1}$ ensures that the current density J should safely vary from 1000 $A m^{-2}$ to 8000 $A m^{-2}$ without local fuel starvation, whereas high P_{mp} , U_f , η_e and η_{tot} can be achieved.

Fig. 8a–d shows the maximum temperature (T_{max}), maximum temperature gradient ($\Delta T/\Delta x_{max}$), x-axis (l) where the T_{max} and $\Delta T/\Delta x_{max}$ occur, respectively, as a function of output current density (J) and velocity of fuel gas ($v_{in,a}$) at the anode inlet. As can be seen in plot a), the T_{max} monotonically increases with increasing the J , which is expected due to increased heat losses. The T_{max} within the SOFC structure is about 50 K higher than the ambient temperature and the temperature of inlet gases (specified with boundary conditions) at $J = 10,000 A m^{-2}$. A similar observation can be made in plot b), since the $\Delta T/\Delta x_{max}$ also increases with increasing the J . The $\Delta T/\Delta x_{max}$ is about 13,500 $K m^{-1}$ at $J = 10,000 A m^{-2}$. As can be seen in plot c), the T_{max} occurs at different location within the SOFC regarding the J and $v_{in,a}$. The T_{max} is shifted from the outlet (at $l = 100 mm$) at $J = 1000 A m^{-2}$ towards the inlet (at $l = 0 mm$) at $J = 10,000 A m^{-2}$.

For example, T_{max} is shifted from $l = 98 mm$ at $J = 1000 A m^{-2}$ to $l = 28 mm$ at $J = 10,000 A m^{-2}$ if $v_{in,a} = 0.5 m s^{-1}$. A slight spatial shift of T_{max} (e.g. from $l = 52.5 mm$ to

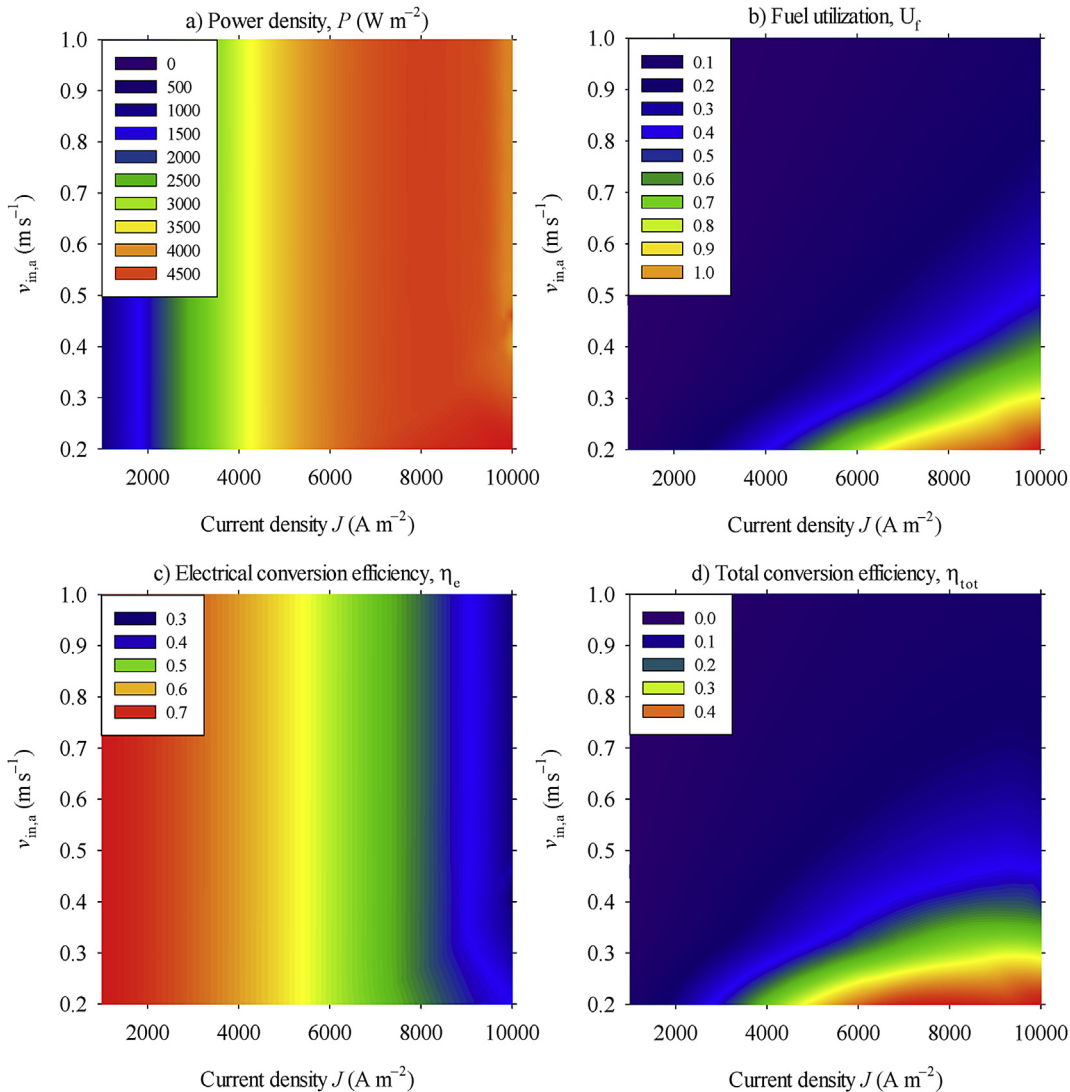


Fig. 7 – a–d): power density (P), fuel utilization (U_f), electrical (η_e) and total conversion efficiency (η_{tot}) of the modeled solid oxide fuel cell (SOFC) as a function of output current density (J) and velocity of fuel gas ($v_{in,a}$) at the anode inlet.

$l = 42.5$ mm at $J = 5700$ A m $^{-2}$) is also observed if $v_{in,a}$ is increased from 0.2 m s $^{-1}$ to 1.0 m s $^{-1}$. It should be stressed that the $\Delta T/\Delta x_{max}$ occurs predominantly at the inlet, but it also occurs at the outlet of the SOFC when the J ranges from 1000 A m $^{-2}$ to 2000 A m $^{-2}$, as can be seen in plot d). Depending on operating conditions, the T_{max} ($\Delta T/\Delta x_{max}$) occurs at different locations within the SOFC. Moreover, the $\Delta T/\Delta y_{max}$ or $\Delta T/\Delta z_{max}$ ($\Delta T/\Delta y_{min}$ or $\Delta T/\Delta z_{min}$) are also very important (not shown in plots) since they may be even higher (lower) than $\Delta T/\Delta x_{max}$ ($\Delta T/\Delta x_{min}$), as shown in this study and also in Ref. [9], so it is necessary to use 3-D model to find out the most critical temperature gradient.

For optimum control, it is crucial to obtain accurate maximum temperature and temperature gradients, and their location. Since the number of thermocouples within a realistic SOFC is limited and the locations, where the thermocouples measure the temperature, are fixed, it is impossible to get the exact values of maximum temperature and temperature

gradients. The presented 3-D model thus gives us valuable data for estimation of maximum temperature and temperature gradients when soft sensors [31] are implemented to control a realistic SOFC more efficiently.

However, a complete control design requires development of the model-based controller, e.g. model predictive control (MPC) [32] might be appropriate for SOFC system, which is needed to capture dynamic behavior during the operation of a realistic SOFC. Future work thus demands implementation of the 3-D dynamic model [33] for single, planar, anode-supported SOFC, including the development of control strategy.

Conclusions

An advanced, three-dimensional (3-D), steady-state, thermo-fluid model of a single, planar, anode-supported, solid oxide

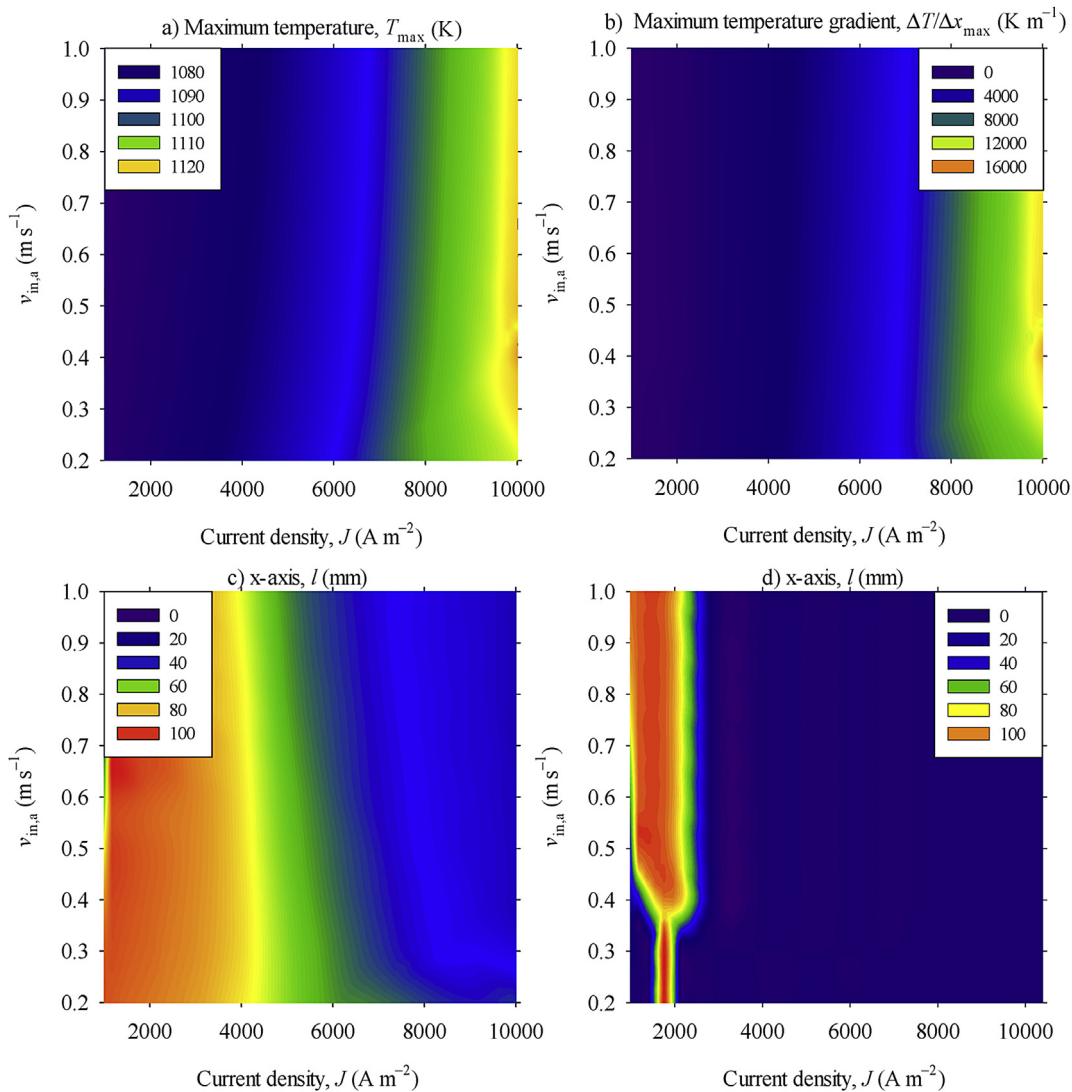


Fig. 8 – a–d): Maximum temperature (T_{max}), maximum temperature gradient ($\Delta T/\Delta x_{max}$), and x-axis (l) where the T_{max} and $\Delta T/\Delta x_{max}$ occur, respectively, as a function of output current density (J) and velocity of fuel gas ($v_{in,a}$) at the anode inlet.

fuel cell (SOFC) has been implemented in software package COMSOL Multiphysics® 4.3 and presented in details. The internal steam reforming of methane and water-gas-shift chemical reactions are considered in the model.

The simulation results show that modeling of the radiative heat transfer is necessary when the SOFC operates at high temperatures, in the range from 800 °C to 1000 °C, since the radiative terms become significant. The power density (P), fuel utilization (U_f), electrical (η_e) and total (η_{tot}) conversion efficiency are studied at different current densities (J) and inlet velocities ($v_{in,a}$) of fuel gas. The simulation results show that the maximum P is not coincident with maximum U_f or η_{tot} if the $v_{in,a}$ is varied. It is also shown that increasing the $v_{in,a}$ beyond 0.3 m s^{-1} has small gain on the maximum P , while the U_f and η_{tot} drop significantly. Conversely, decreasing the $v_{in,a}$ below 0.2 m s^{-1} lowers the maximum P . It can be concluded that the J and $v_{in,a}$ have to be controlled precisely to obtain

maximum P , U_f , η_e and η_{tot} if it is considered that the inlet composition of fuel gas is fixed. The latter should be varied with special care in practice since the steam-to-carbon ratio (STCR) has to be higher than two to prevent solid carbon deposition. Various inlet compositions of fuel gas should be addressed in the next paper by considering also the influence of SOFC's geometry on the performance parameters. The results also show that the maximum temperature (T_{max}) and maximum temperature gradient ($\Delta T/\Delta x_{max}$) occur at different locations within the SOFC depending on the J and $v_{in,a}$. The presented model thus helps to predict the T_{max} ($\Delta T/\Delta x_{max}$) and its location within the SOFC. The most important gain is valuable data for efficient control of a realistic SOFC with reduced number of thermocouples for temperature measurements. However, dynamic model of the SOFC is needed to develop appropriate control strategy. The future work will focus on dynamic modeling and control of a realistic SOFC.

Acknowledgments

The authors acknowledge the support of the Slovenian Research Agency through the Programme P2-0001.

REFERENCES

- [1] Costamagna P, Selimovic A, Del Borghi M, Agnew G. Electrochemical model of the integrated planar solid oxide fuel cell (IP-SOFC). *Chem Eng J* 2004;102:61–9.
- [2] Janardhanan VM, Deutschmann O. Modeling of solid-oxide fuel cells. *Z Phys Chem* 2007;221:443–78.
- [3] Kakaç S, Pramanjaroenkij A, Zhou XY. A review of numerical modeling of solid oxide fuel cells. *Int J Hydrogen Energy* 2007;32:761–86.
- [4] EG & G Technical Services Inc. Science applications international corporation. Fuel cell handbook. 6th ed. Morgantown, WV: US Department of Energy, Office of Fossil Energy, National Energy Technology Laboratory; November 2002.
- [5] Petrucci L, Cocchi S, Fineschi F. A global thermo-electrochemical model for SOFC systems design and engineering. *J Power Sour* 2003;118:96–107.
- [6] Aguiar P, Adjiman CS, Brandon NP. Anode-supported intermediate temperature direct internal reforming solid oxide fuel cell. I: model-based steady-state performance. *J Power Sour* 2004;138:120–36.
- [7] Lehnert W, Meusinger J, Thom F. Modelling of gas transport phenomena in SOFC anodes. *J Power Sour* 2000;87:57–63.
- [8] Khaleel MA, Lin Z, Singh P, Surdoval W, Collin D. A finite element analysis modeling tool for solid oxide fuel cell development: coupled electrochemistry, thermal and flow analysis in MARC®. *J Power Sour* 2004;130:136–48.
- [9] Nikooyeh K, Jeje AA, Hill JM. 3D modeling of anode-supported planar SOFC with internal reforming of methane. *J Power Sour* 2007;171:601–9.
- [10] Akhtar N, Decent SP, Loghin D, Kendall K. A three-dimensional numerical model of a single-chamber solid oxide fuel cell. *Int J Hydrogen Energy* 2009;34:8645–63.
- [11] Bertei A, Mertens J, Nicolella C. Electrochemical simulation of planar solid oxide fuel cells with detailed microstructural modeling. *Electrochim Acta* 2014;146:151–63.
- [12] Ott J, Völker B, Gan Y, McMeeking RM, Kamlah M. A micromechanical model for effective conductivity in granular electrode structures. *Acta Mech Sin* 2013;29(5):682–98.
- [13] Qu Z, Aravind PV, Dekker NJJ, Janssen AHH, Woudstra N, Verkooijen AHM. Three-dimensional thermo-fluid and electrochemical modeling of anode-supported planar solid oxide fuel cell. *J Power Sour* 2010;195:7787–95.
- [14] Andreassi L, Rubeo G, Ubertini S, Lunghi P, Bove R. Experimental and numerical analysis of a radial flow solid oxide fuel cell. *Int J Hydrogen Energy* 2007;32:4559–74.
- [15] Trengove RD, Wakeham WA. The viscosity of carbon monoxide, methane and sulfur hexafluoride in the limit of zero density. *J Phys Chem Ref Data* 1987;16(2):175–87.
- [16] Vogel E. Towards reference viscosities of carbon monoxide and nitrogen at low density using measurements between 290 K and 680 K as well as theoretically calculated viscosities. *Int J Thermophys* 2012;33:741–57.
- [17] Uribe FJ, Mason EA, Kestin J. Thermal conductivity of nine polyatomic gases at low density. *J Phys Chem Ref Data* 1990;19(5):1123–36.
- [18] Fuller EN, Schettler PD, Giddings JC. A new method for prediction binary gas-phase diffusion coefficients. *Ind Eng Chem* May 1966;58(5).
- [19] Das T, Narayanan S, Mukherjee R. Steady-state and transient analysis of a steam-reformer based solid oxide fuel cell system. *J Fuel Cell Sci Technol* 2010;7. 011022–1.
- [20] Cui D, Liu L, Dong Y, Cheng M. Comparison of different current collecting modes of anode supported micro-tubular SOFC through mathematical modeling. *J Power Sour* 2007;174:246–54.
- [21] Xie Y, Ding H, Xue X. Direct methane fueled solid oxide fuel cell model with detailed reforming reactions. *Chem Eng J* 2013;228:917–24.
- [22] Janardhanan VM, Deutschmann O. CFD analysis of a solid oxide fuel cell with internal reforming: coupled interactions of transport, heterogeneous catalysis and electrochemical processes. *J Power Sour* 2006;162:1192–202.
- [23] Gazzari JI, Kesler O. Non-destructive delamination detection in solid oxide fuel cells. *J Power Sour* 2007;167:430–41.
- [24] ThyssenKrupp VDM, Crofer® 22 H, Preliminary Material Data Sheet No. 4050 June 2008 Edition.
- [25] Zhu H, Kee RJ. A general mathematical model for analyzing the performance of fuel-cell membrane-electrode assemblies. *J Power Sour* 2003;117:61–74.
- [26] Robinson JB, Brown LD, Jervis R, Taiwo OO, Heenan TMM, Millichamp J, et al. Investigating the effect of thermal gradients on stress in solid oxide fuel cell anodes using combined synchrotron radiation and thermal imaging. *J Power Sour* 2015;288:473–81.
- [27] Lin C-K, Liu Y-A, Wu S-H, Liu C-K, Lee R-Y. Joint strength of a solid oxide fuel cell glass-ceramic sealant with metallic interconnect in a reducing environment. *J Power Sour* 2015;280:272–88.
- [28] Matsuzaki Y, Baba Y, Sakurai T. High electric conversion efficiency and electrochemical properties of anode-supported SOFCs. *Solid State Ionics* 2004;174:81–6.
- [29] Chen S, Lior N, Xiang W. Coal gasification integration with solid oxide fuel cell and chemical looping combustion for high-efficiency power generation with inherent CO₂ capture. *Appl Energy* 2015;146:298–312.
- [30] Bunin GA, Wuillemin Z, François G, Nakajo A, Tsikonis L, Bonvin D. Experimental real-time optimization of a solid oxide fuel cell stack via constraint adaptation. *Energy* 2012;39:54–62.
- [31] Kadlec P, Gabrys B, Strandt S. Data-driven soft sensors in the process industry. *Comput Chem Eng* 2009;33:795–814.
- [32] Sanandaji BM, Vincent TL, Colclasure AM, Kee RJ. Modeling and control of tubular solid-oxide fuel cell systems: II. Nonlinear model reduction and model predictive control. *J Power Sour* 2011;196:208–17.
- [33] Aguiar P, Adjiman CS, Brandon NP. Anode-supported intermediate-temperature direct internal reforming solid oxide fuel cell II. Model-based dynamic performance and control. *J Power Sour* 2005;147:136–47.